Nanoscale

PAPER

View Article Online
View Journal | View Issue

Cite this: *Nanoscale*, 2018, **10**, 19484

A three-dimensional nickel–chromium layered double hydroxide micro/nanosheet array as an efficient and stable bifunctional electrocatalyst for overall water splitting†

Wen Ye, Xiaoyu Fang, Xuebo Chen * and Dongpeng Yan *

Received 24th July 2018,
Accepted 24th September 2018

DOI: 10.1039/c8nr05974h

rsc.li/nanoscale

The development of bifunctional and stable non-noble metal electrocatalysts for the high-performance hydrogen evolution reaction (HER) and oxygen evolution reaction (OER) is very important and challenging for renewable energy. Herein, for the first time, a nickel–chromium layered double hydroxide (NiCr-LDH) nanosheet array was developed as a bifunctional electrocatalyst towards overall water splitting. By tuning different Ni/Cr ratios of LDHs, the optimized Ni_2Cr_1-LDH shows extraordinary HER activity with an ultra-low overpotential of 138 mV at 100 mA cm^{-2}, compared with all of the reported Ni-based LDHs (NiFe-LDH, NiCo-LDH, NiMn-LDH, NiTi-LDH, NiV-LDH *etc.*) and even outperforming Pt/C catalysts. The small overpotential of 319 mV at 100 mA cm^{-2} for the OER and outstanding durability at 1.55 V (*vs.* RHE) for 30 hours can also be achieved for Ni_2Cr_1-LDH. Notably, a two-electrode electrolyzer with a Ni_2Cr_1-LDH bifunctional electrocatalyst as both the anode and the cathode can work for at least 30 hours with a cell voltage of merely 1.55 V at 10 mA cm^{-2}. Both experimental and density functional theoretical calculations show that the Cr^{3+} ions within the LDH layer serve as charge transfer sites and thus effectively boost the intrinsic electrochemical activity. Therefore, this work provides a new NiCr-LDH system as a more efficient metal hydroxide for bifunctional water splitting electrocatalyst.

Introduction

Electrocatalytic water splitting into hydrogen and oxygen is considered to be a promising way to achieve efficient, clean, sustainable energy conversion and storage.[1–3] Generally, the electrochemical water splitting contains two half reactions, namely the oxygen evolution reaction (OER) at the anode and the hydrogen evolution reaction (HER) at the cathode.[4–6] During the last few years, many excellent electrocatalysts have been studied to increase the reaction rate and to reduce the overpotential, in which the representative systems are the noble metal based catalysts. However, these systems (such as Pt, RuO_2 and IrO_2) usually restrict their wide application in practice due to their high price and scarcity.[7–9] Therefore, searching for new Earth-abundant, highly active and stable non-noble metal electrocatalysts has attracted much recent interest.

Layered double hydroxide (LDH), also known as an anionic or hydratalcite-like clay, consists of layers of divalent and trivalent metal cations coordinated with hydroxide ions, accompanied by guest anion (CO_3^{2-}, Cl^-, *etc.*) intercalation between the layers. The two-dimensional (2D) layered structure endows the LDH systems with essential charge transport properties, which have been widely used in electrocatalysis.[10–13] Particularly, benefitting from the Earth abundance and highly active OER activities, Ni-based LDHs (such as NiFe-LDH,[14–19] NiCo-LDH,[20] NiMn-LDH,[21] NiFeMn-LDH,[22] NiTi-LDH,[23] NiV-LDH[24] *etc.*) are considered as promising candidates. Furthermore, to enhance the electrochemical activities, several fabrication strategies have been developed. Firstly, to increase the number of active sites, hierarchical structures and micro/nanosheets have been constructed by the modification of the electrode. For example, due to the large porosity and good conductivity, many transition metal electrodes (such as nickel foam (NF)) have been selected as substrates.[20,25–30] By direct growth of 2D LDH materials on these three-dimensional (3D) porous conductive substrates, highly active and stable electroactive catalysts can be designed. Secondly, the combination of both intrinsic electrochemical activity and high charge transfer of each catalytic site also became a major way. However, as is known, Ni or Co hydroxide is almost an insulator and causes

Beijing Key Laboratory of Energy Conversion and Storage Materials, College of Chemistry, Beijing Normal University, Beijing 100875, People's Republic of China. E-mail: yandongpeng001@163.com, yandp@bnu.edu.cn, xuebochen@bnu.edu.cn

†Electronic supplementary information (ESI) available. See DOI: 10.1039/c8nr05974h

poor charge transfer properties during the water splitting reaction.[31,32] If the conductivity of the electrocatalysts can be increased, it will inevitably benefit the increase of reaction activity and reusability. From an elemental point of view, the Cr^{3+} cation presents a special electronic configuration ($t^3_{2g}e^0_g$), which facilitates charge transfer and electron capture.[33] Thus, the incorporation of Cr^{3+} into Ni or Co hydroxide would be expected to increase the conductivity. As well, Cr^{3+} ions are easily oxidized to higher oxidation states during the OER, which in turn has a positive effect on the water oxidation active species (such as Co or Ni sites). For example, it has been reported that the addition of Cr^{3+} can increase the OER performance of Co-based LDH catalysts.[34] Additionally, Jin and co-workers incorporated Cr into NiFe-LDH to improve the OER performance.[35] However, whether Cr-containing LDHs could achieve high-efficiency electrocatalysis for both the OER and HER has not been investigated yet.

To develop new 2D efficient bifunctional electrocatalysts, in this work, we selected NiCr-LDHs as model systems, which have not been studied towards electrocatalytic overall water splitting before this work. A facile one-step hydrothermal method was developed to directly grow the 2D NiCr-LDH micro/nanosheet array onto 3D porous conductive NF, which could serve as a novel bifunctional catalyst for full water splitting for the first time. As a result, the developed Ni_2Cr_1-LDH electrode presents superior HER activity with ultralow overpotentials of 67 and 138 mV at 10 and 100 mA cm^{-2}, respectively, which are much lower than the values for majority of the reported Ni-based LDHs (such as NiFe-LDH,[26] NiCo-LDH,[20] NiMn-LDH,[21] *etc.*). Moreover, the excellent OER activity of Ni_2Cr_1-LDH (an overpotential value of 319 mV at 100 mA cm^{-2}) could also be achieved. Notably, the two-electrode configuration cell with the Ni_2Cr_1-LDH electrocatalyst can work for a long period of time at a voltage of 1.55 V and deliver a current density of 10 mA cm^{-2}. Therefore, this work not only develops new types of NiCr-LDHs as bifunctional catalysts, but also provides new insight into the role of Cr^{3+} ions for promoting the electrochemical activities of the LDH layer.

Results and discussion

The NiCr-LDH samples with different Ni/Cr ratios (from 1 : 1 to 4 : 1) were prepared, in which the products are noted as Ni_xCr_y-LDHs, where x and y stand for the relative feeding amount of Ni and Cr, respectively. XRD was firstly employed to confirm the structure of NiCr-LDH. As shown in Fig. 1, except for the peaks marked by pentacles belonging to NF, the diffraction peaks appear at 11.4°, 23.3°, 34.0°, and 60.8°, which can be assigned to the characteristic (003), (006), (009) and (110) facets of the LDH, respectively. These results strongly prove the successful fabrication of NiCr-LDH on the NF substrate.[21,36] The interlayer spacing can be estimated as *ca.* 0.79 nm, corresponding to the CO_3^{2-} intercalated LDHs. Additionally, the relatively weak intensity and wider peak of (00l) diffractions indicate that the crystal degrees of LDHs are low, with thin 2D sheet-like structures.[11]

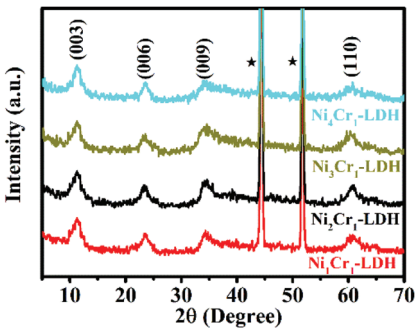

Fig. 1 XRD patterns of Ni_1Cr_1-LDH, Ni_2Cr_1-LDH, Ni_3Cr_1-LDH and Ni_4Cr_1-LDH. The peaks marked by pentacle symbols are indexed to NF.

Next, the morphology of the Ni_xCr_y-LDH samples was characterized by SEM. Numerous nanosheets with a size of *ca.* 100 nm and a thickness of *ca.* 20 nm were uniformly grown on the NF (Fig. 2a and S1–S4a, b†). The corresponding EDS analysis further discloses that the chemical compositions of Ni_xCr_y-LDHs (Fig. S1–S4c†) are consistent with the different feeding ratios. Furthermore, TEM images (Fig. 2b) confirm the nanosheet-like structure of Ni_2Cr_1-LDH. The high-resolution TEM image (inset in Fig. 2b) reveals that the interplanar spacing is 0.155 nm,[37] which corresponds well with the d spacing of the (110) plane of the typical LDH structure.[11] The EDS mapping on the typical Ni_2Cr_1-LDH nanosheets verifies the homogeneous elemental distributions (Fig. 2c–g and Fig. S5†) of Ni, Cr, O and C compositions.

To study the surface chemical states of Ni_2Cr_1-LDH, XPS was further performed. As shown in Fig. 3a, two strong peaks of Ni 2p at 856.0 and 873.6 eV are assigned to the binding

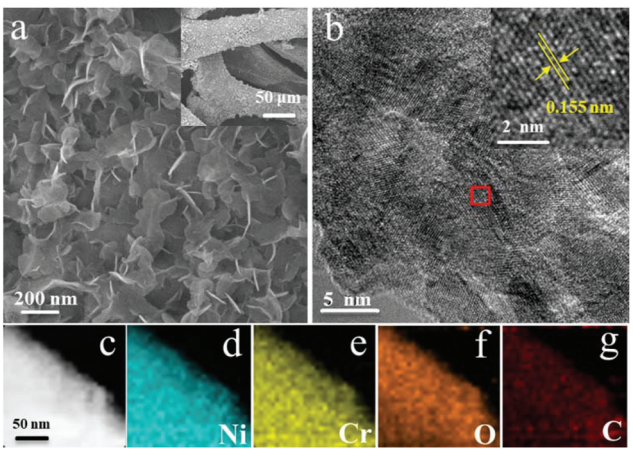

Fig. 2 (a) SEM image of Ni_2Cr_1-LDH. The inset in panel (a) is the low-resolution SEM image of Ni_2Cr_1-LDH on the NF. (b) TEM image of Ni_2Cr_1-LDH. The inset in panel (b) is the high-resolution TEM image of the selected area in (b) marked by a red line and (c) low-resolution HAADF-STEM images of Ni_2Cr_1-LDH. The corresponding elemental mapping images of (d) Ni, (e) Cr, (f) O, and (g) C in Ni_2Cr_1-LDH.

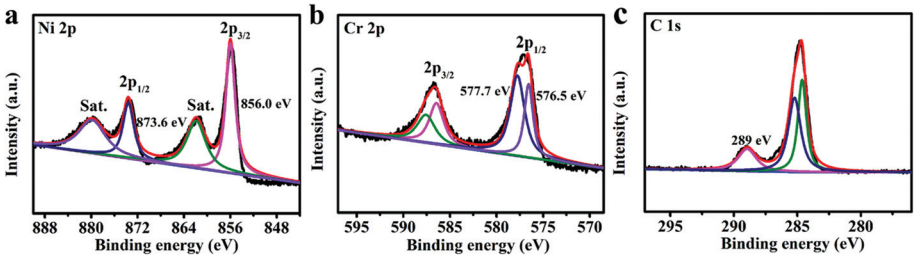

Fig. 3 High-resolution XPS spectra of the Ni 2p, Cr 2p and C 1s core levels for Ni_2Cr_1-LDH.

energies of Ni $2p_{3/2}$ and Ni $2p_{1/2}$, respectively, indicating the existence of Ni(II) in Ni_2Cr_1-LDH.[38,39] In the Cr 2p spectrum (Fig. 3b), two broad peaks located at 586.4 and 577.1 eV correspond to Cr $2p_{1/2}$ and Cr $2p_{3/2}$, respectively. The peak at 577.7 eV is attributed to Cr^{3+} hydroxide, which also confirms that Cr ions are trivalent.[40] The binding energy of Cr 2p at 577.7 and 576.5 eV suggests the formation of Cr–OH and Cr–O chemical bonds, respectively.[34,41] The C 1s spectrum (Fig. 3c) at the main peak with a high binding energy at 289 eV corresponds to O–C=O in CO_3^{2-}, which demonstrates the presence of CO_3^{2-} intercalation in the LDH layer. Therefore, the XPS results confirm that the as-obtained NiCr-LDH nanosheets were stably grown on the NF.

The electrochemical HER performances for different NiCr-LDHs during water splitting were studied. All of the electrochemical measurements were applied in a standard three-electrode system with an electrolyte solution of 1.0 M KOH. The polarization curves with *iR* compensation are shown in Fig. 4a. As a comparison, the bare NF and RuO_2 were also tested under the same conditions. Ni_4Cr_1-LDH exhibits an overpotential of 88 mV at 10 mA cm^{-2}, which is much smaller than bare NF (186 mV at 10 mA cm^{-2}). Among the NiCr-LDHs, Ni_2Cr_1-LDH exhibits the smallest onset potential for the HER (67 mV at 10 mA cm^{-2}) in contrast to the Ni_1Cr_1 (83 mV at 10 mA cm^{-2}), Ni_3Cr_1 (82 mV at 10 mA cm^{-2}) and bare NF, while it is larger than Pt/C (51 mV at 10 mA cm^{-2}). It is worth noting that, regardless of the proportion of NiCr-LDH materials, the overpotentials under 100 mA cm^{-2} are much less than the Pt/C electrode. Compared with Pt/C (195 mV at 100 mA cm^{-2}), Ni_2Cr_1-LDH reveals an overpotential of merely 138 mV. The excellent performance of the NiCr-LDH catalyst suggests the more effective mass transport and faster reaction kinetics in the HER. Such performance is also comparable to the recently reported HER electrocatalysts such as Ni@NC (≈300 mV at 100 mA cm^{-2}),[42] Co_xNi_yP NTs (≈490 mV at 100 mA cm^{-2}),[43] $NiCo_2S_4$ (≈350 mV and 245 mV at 100 mA cm^{-2}),[27] Ni_5P_4 (≈323 mV at 100 mA cm^{-2}),[44] VOOH (≈270 mV at 100 mA cm^{-2}),[45] porous $NiFe/NiCo_2O_4$/NF (200 mV at 100 mA cm^{-2}),[28] $NiFeO_x$/CFP (≈230 mV at 100 mA cm^{-2})[46] and Ni_3S_2/NF (≈400 mV at 100 mA cm^{-2})[47] (Table S1†). Furthermore, the Tafel slope of Ni_2Cr_1-LDH is 61.5 mV dec^{-1}, which is much lower than that of Ni_1Cr_1-LDH (72.2 mV dec^{-1}), Ni_3Cr_1-LDH (62.2 mV dec^{-1}), Ni_4Cr_1-LDH (80.1 mV dec^{-1}), bare NF (136.9 mV dec^{-1}) and even Pt/C (64.2 mV dec^{-1}), as shown in Fig. 4b. The long-term durability of the catalyst is also a critical parameter, and thus we further carried out a durability test of the Ni_2Cr_1-LDH electrode. The *I–t* curve (Fig. 4c) shows that the catalytic current density exhibits a numerical retention after 30 h of continuous measurement under a constant potential of −0.07 V *versus* RHE, suggesting its outstanding durability.

For the OER process on Ni_xCr_y-LDH electrodes, the electrocatalytic activity shows a similar trend to the HER. The polarization curves with *iR* compensation are shown in Fig. 5a. The oxidation peak at about 1.4 V for all NiCr-LDHs is due to the oxidation state of Ni from bivalent to trivalent to form NiOOH.[27,48,49] It has been confirmed that in the OER process, the catalytically active site of the Ni-based catalyst is located in the structure of NiOOH, which plays a vital role in the OER activity.[50] The bare NF shows poor OER properties, while RuO_2 presents a large overpotential of 420 mV at 50 mA cm^{-2}. In contrast, Ni_4Cr_1-LDH exhibits the preferable OER performance

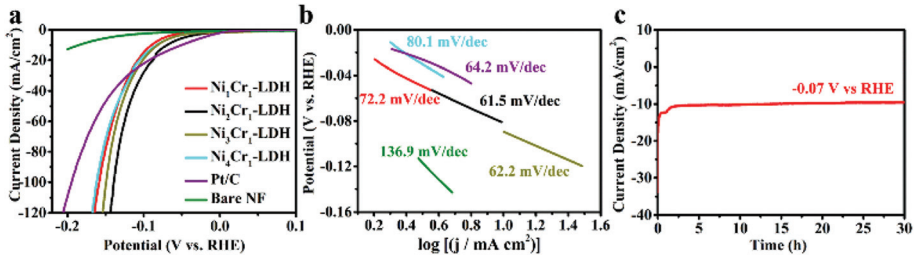

Fig. 4 (a) HER polarization curves and (b) polarization curve derived Tafel plots of Ni_1Cr_1-LDH, Ni_2Cr_1-LDH, Ni_3Cr_1-LDH, Ni_4Cr_1-LDH, RuO_2, and bare Ni foam. (c) Time dependence of current density under a constant potential of −0.07 V *versus* RHE of Ni_2Cr_1-LDH.

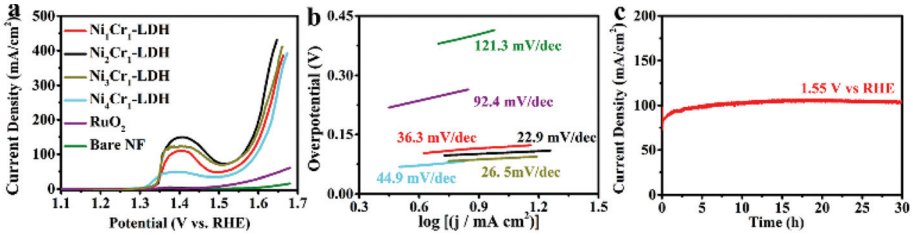

Fig. 5 (a) OER polarization curves and (b) polarization curve derived Tafel plots of Ni_1Cr_1-LDH, Ni_2Cr_1-LDH, Ni_3Cr_1-LDH, Ni_4Cr_1-LDH, RuO_2, and bare Ni foam. (c) Time dependence of current density under a constant potential of 1.55 V *versus* RHE of Ni_2Cr_1-LDH.

in terms of the overpotential of 364 mV at 100 mA cm^{-2}. The increased activity of Ni_1Cr_1-LDH, Ni_2Cr_1-LDH and Ni_3Cr_1-LDH can be observed apparently from the negative shift of the LSV curve. It is worth noting that the Ni/Cr ratio of 2 : 1 achieves the highest OER activity in terms of the lowest overpotentials of 319 mV and 390 mV at 100 and 300 mA cm^{-2}, respectively. Remarkably, the η_{100} value for Ni_2Cr_1-LDH is comparable to those of other state-of-the-art OER catalysts, such as $NiCo_2O_4$,[51] FeNi@single layer graphene,[52] VOOH[45] and CoMnCH[25] (Table S2†), and is much smaller than those of the reported systems for Ni-based LDHs (460 mV,[26] ≈320 mV,[17] ≈420 mV (ref. 20) and 349 mV (ref. 25) at 100 mA cm^{-2}). Such good performance can be related to the orientational growth of 2D LDH nanosheets onto the 3D networks, which not only provides a large surface area, but also exposes more accessible active sites contributing to high current densities. Fig. 5b presents the Tafel plots derived from the corresponding LSV curves. The bare NF and RuO_2 deliver the Tafel slope of 121.3 and 92.4 mV dec^{-1}, respectively. These values are larger than those of Ni_1Cr_1-LDH (36.3 mV dec^{-1}), Ni_3Cr_1-LDH (26.5 mV dec^{-1}) and Ni_4Cr_1-LDH (44.9 mV dec^{-1}), while Ni_2Cr_1-LDH shows the lowest Tafel slope of 22.9 mV dec^{-1}, suggesting that Ni_2Cr_1-LDH has favorable kinetics of electrochemical water oxidation. Furthermore, the stability was tested under a constant potential of 1.55 V *versus* RHE for 30 hours, and the catalytic current density displays even a slight increase, implying the high stability of the electrocatalysis (Fig. 5c and S6†). XPS was conducted to investigate the changes in the surface composition of the NiCr-LDH catalyst after OER catalysis. Fig. S7† shows the Ni 2p and Cr 2p XPS spectra of the post-OER Ni_2Cr_1-LDH sample. As shown in Fig. S7a,† the Ni 2p XPS spectrum shows a new signal for NiOOH, which is located at 857.9 eV after OER catalysis.[38] Moreover, XPS spectroscopy of Cr species indicates that there is no additional peak after OER measurement (Fig. S7b†). Since the oxidation of Ni changes the local chemical environment, Cr 2p is slightly shifted to a higher binding energy. This slight change in the surface valence state is consistent with the high stability of the Ni_2Cr_1-LDH electrode.

The above experiments show that the overpotentials of both the HER and OER are the lowest when the Ni/Cr ratio in NiCr-LDH is 2 to 1. To better understand the factors influencing the highly enhanced catalytic activity of Ni_2Cr_1-LDH relative to other electrodes, the electrochemically active surface areas (ECSA) of NiCr-LDH with different Ni/Cr ratios were evaluated by measuring the double-layer capacitances (C_{dl}) through collecting CV in a non-faradaic potential range of 1.05–1.15 V *vs.* RHE at different scan rates (Fig. S8a–d†). It is generally accepted that the ECSA of the electrode materials is proportional to their C_{dl} value, which is given by the linear slope of the current density *vs.* the scan rate curve. The calculated ESCAs of different Ni/Cr ratios are shown in Fig. S8e.† The C_{dl} value of Ni_2Cr_1-LDH is 22.9 mF cm^{-2}, which is about 2.1 times, 1.4 times and 3.3 times higher than those of Ni_1Cr_1-LDH (10.8 mF cm^{-2}), Ni_3Cr_1-LDH (16.3 mF cm^{-2}) and Ni_4Cr_1-LDH (6.9 mF cm^{-2}), respectively. The current density of the NiCr-LDH samples can be normalized to their corresponding ECSAs for a reasonable comparison. The higher ECSA of Ni_2Cr_1-LDH reveals that it has the largest effective surface area. Obviously, NiCr-LDH with the highest ECSA value of 2 : 1 exhibits the best HER and OER activities. Turnover frequency (TOF) is also a key kinetic parameter for the OER, indicating the intrinsic properties of the electrocatalytic activity. Here, it is assumed that all metal sites in NiCr-LDH are electrochemically active in the water oxidation reaction, and their turnover frequencies at an overpotential of 400 mV can be calculated. Ni_2Cr_1-LDH shows a much higher TOF (0.119 s^{-1}), which is approximately 1.1, 1.3, and 1.6 times higher than the corresponding values for Ni_3Cr_1-LDH (0.112 s^{-1}), Ni_1Cr_1-LDH (0.091 s^{-1}), and Ni_4Cr_1-LDH (0.073 s^{-1}), respectively. It is worth mentioning that the above-mentioned TOFs are obviously underestimated because some metal sites may be electrochemically inaccessible.

To confirm the role of Cr^{3+} in the excellent HER and OER activities of NiCr-LDH, $Ni(OH)_2$ and $Cr(OH)_3$ were also prepared to compare with NiCr-LDH under the same experimental conditions (Fig. S9†).[26] We also investigated the HER and OER activities of $Ni(OH)_2$ and $Cr(OH)_3$ onto the NF electrode. As shown in Fig. S10a,† the current density of Ni_2Cr_1-LDH at −0.1 V (*vs.* RHE) is 27.8 mA cm^{-2} for the HER, which is 6.8 times larger than that of $Ni(OH)_2$ (4.1 mA cm^{-2}) and 55.6 times larger than that of $Cr(OH)_3$ (0.5 mA cm^{-2}). Meanwhile, the current density of Ni_2Cr_1-LDH at 1.6 V (*vs.* RHE) is 208.6 mA cm^{-2} for the OER, which is 11.3 times larger than that of $Ni(OH)_2$ (18.4 mA cm^{-2}) and 29.4 times larger than that of $Cr(OH)_3$ (7.1 mA cm^{-2}) as shown in Fig. S10b.† Moreover, the capacitance values of Ni_2Cr_1-LDH, $Ni(OH)_2$ and $Cr(OH)_3$ are 22.9 mF cm^{-2}, 1.8 mF cm^{-2} and 1.1 mF cm^{-2},

respectively (Fig. S11†), suggesting that NiCr-LDH has the highest electrochemical surface area. More importantly, the conductivity of Ni_2Cr_1-LDH, $Ni(OH)_2$ and $Cr(OH)_3$ was evaluated by electrochemical impedance spectroscopy (EIS). The Nyquist plots of the three electrodes show a significant semicircle in the high frequency range that can be correlated with the charge transfer resistance (R_{ct}) of the LDH catalysts. Fig. S12† shows that Ni_2Cr_1-LDH possesses the smallest R_{ct} (0.51 Ω) in contrast to that for $Ni(OH)_2$ (7.04 Ω) and $Cr(OH)_3$ (12.09 Ω), suggesting that the doping of Cr^{3+} can increase the intrinsic conductivity and the electron transfer efficiency, and thus further improve the catalytic performance of the OER. These results clearly demonstrate that NiCr-LDH exhibits superior performance relative to the pristine $Ni(OH)_2$ and $Cr(OH)_3$.

Diaz-Morales *et al*. believe that the catalytically active site of NiCr-LDH is considered to be the Ni ion rather than the Cr site.[53] It is well known that nickel hydroxide is almost an insulator, which results in poor reactivity due to poor charge transfer properties in the reaction.[54] If the conductivity of the material is increased, the electrochemical activity will inevitably increase. In order to detect the role of Cr^{3+} in the LDH layer, periodic density functional theoretical (PDFT) calculations were performed on idealized models of Ni_2Cr_1-LDH.[55] The calculated band gap is *ca.* 0.178 eV, suggesting the highly conductive properties. The total and partial electronic densities of state (TDOS and PDOS, respectively, Fig. 6 and Fig. S13†) show that the top of the valence band (TVB) of NiCr-LDH is populated with both Cr and Ni electrons, while the bottom of the conducting band (BCB) is mainly contributed by the 3d atomic orbitals of Cr, suggesting the potential electronic transfer between $Ni(OH)_2$ and adjacent $Cr(OH)_3$ as well as the strong electron conductivity in the NiCr-LDH layer. The PDOS profiles of majority spin and minority spin for both Ni and Cr metals present an unsymmetrical distribution, which indicates that the electron spin-polarization between Ni^{2+} and Cr^{3+} may also play an important role in the electronic transport, which is consistent with NiCr-LDH that presents a high electrocatalytic activity during the OER and HER in experiment. Additionally, the calculated models for Ni_3Cr_1-LDH and Ni_5Cr_1-LDH were further analyzed (Fig. S14 and S15†), in which the TDOS/PDOS and the band gap are very similar to those of Ni_2Cr_1-LDH.

In view of the excellent OER and HER performances of bifunctional NiCr-LDH, the overall splitting of water was tested in a two-electrode configuration cell (Video S1†). It is observed that the Ni_2Cr_1-LDH bifunctional electrocatalyst requires a cell voltage of merely 1.55 V to deliver a current density of 10 mA cm^{-2} (Fig. 7). Such a low overpotential of the LDH electrocatalyst for overall water splitting is impressive and comparable to the lowest values for the recently reported overall water splitting materials including NiFe-LDH (1.7 V at 10 mA cm^{-2}),[26] CoMnCH (1.68 V at 10 mA cm^{-2}),[25] Ni_5P_4 (1.7 V at 10 mA cm^{-2}),[44] VOOH (1.62 V at 10 mA cm^{-2}),[45] NiSe/NF (1.63 V at 10 mA cm^{-2})[56] and CoP (1.62 V at 10 mA cm^{-2})[57](Table S3†). More worth emphasizing is that the Ni_2Cr_1-LDH//Ni_2Cr_1-LDH electrolyzer of the two-electrode configuration shows much higher durability after 30 hour long-term measurement. The morphology and the corresponding EDS mapping images of Ni_2Cr_1-LDH after the durability test were also collected (Fig. S16†). Even in the case of a long durability test, it is obvious that the nanosheet array structure is maintained very well, consistent with its stable water splitting performance. The EDS mapping results also suggest the homogeneous distribution of Ni, Cr, O, and C elements. These results promise Ni_2Cr_1-LDH as a new type of electrocatalyst for practical overall water splitting in alkaline media.

Based on both experiment and theoretical calculations, in our opinion, the high OER/HER performance and good stability of NiCr-LDH can be attributed to the following points: (i) the 3D porous structure closely organizes the hierarchical 2D active nanosheets, which could expose more active sites, and facilitate charge transport and gas release in the hierarchical architecture; (ii) the synergistic effect of redox-active cations (Ni and Cr) and Lewis-acid cations (Cr) could enhance the elec-

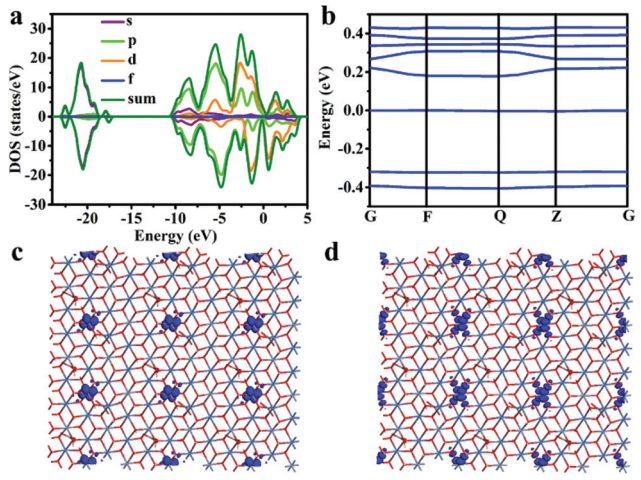

Fig. 6 (a) PDOS/TDOS and (b) the band structure for the Ni_2Cr_1-LDH systems; (c) HOMO and (d) LUMO distributions. G (0,0,0), Z (0,0,1/2), F (0,1/2,0) and Q (1/2,0,0) are the selected reciprocal points in the first Brillouin Zone (BZ).

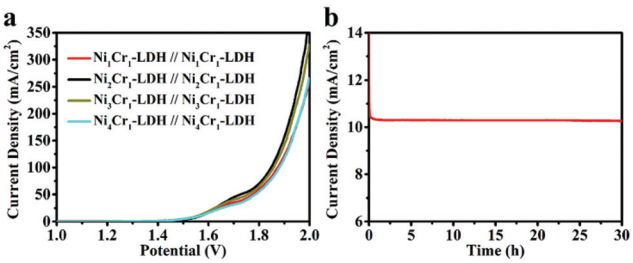

Fig. 7 (a) LSV plots of overall water splitting at Ni_1Cr_1-LDH//Ni_1Cr_1-LDH, Ni_2Cr_1-LDH//Ni_2Cr_1-LDH, Ni_3Cr_1-LDH//Ni_3Cr_1-LDH and Ni_4Cr_1-LDH//Ni_4Cr_1-LDH as cathodes and anodes, respectively. (b) Time-dependent current density curve of Ni_2Cr_1-LDH with a two-electrode configuration under a constant potential of 1.55 V for 30 h, 1 M KOH, pH 14.

tronic interaction in the metal hydroxide matrix, and have a positive effect on the activity of electrocatalytic reactions: redox active cations (Ni^{3+}/Ni^{4+}) with a high oxidation state are believed to be potentially active sites in the NiCr-LDH OER catalyst. The addition of Cr^{3+} cations with a trivalent oxidation state can also buffer the multi-electron processes required for water oxidation. In the LDH layer, the metal cations are bonded to each other through bridged hydroxyl bonds. Cr^{3+} as Lewis acid cations can modulate the ligand fields of these hydroxyl groups; (iii) the Cr^{3+} cation presents a unique electronic configuration ($t^3_{2g}e^0_g$), which facilitates charge transfer, conductivity and electron capture. Different from the previously studied Ni-based LDHs, such as NiFe-, NiCo-, NiMn-, NiTi-, and NiV-LDH, this work demonstrates the improved intrinsic activity of the electrocatalysts by designing the suitable catalyst composition (Cr^{3+} cation) and the effect of high-active-area nanostructures with optimized open frameworks on the overall water splitting performance.

Conclusions

In summary, new types of 2D NiCr-LDH nanosheet arrays with 3D porous microstructures were synthesized through a simple and one-step hydrothermal method, which were further used as bifunctional catalysts towards the overall water splitting. The NiCr-LDHs serve as efficient and stable bifunctional catalysts for electrocatalytic water oxidation and reduction, in which the optimized Ni_2Cr_1-LDH shows an ultralow overpotential of 67 mV at 10 mA cm^{-2} for the HER, 319 mV at 100 mA cm^{-2} for the OER and excellent long-term durability in alkaline media, which is superior to the most current Ni-based LDH electrocatalysts. The combination of experiments and DFT calculations provides a basic understanding of their electronic structures and spin-polarization, confirming the role of Cr-based LDH in the high electron conductivity for the HER and OER processes. Furthermore, a two-electrode configuration cell using Ni_2Cr_1-LDH as both the anode and cathode indicated a practical setup for efficient and stable overall water splitting with a cell voltage of merely 1.55 V to deliver a current density of 10 mA cm^{-2}. It can be expected that the NiCr-LDH nanosheet based electrocatalysts with high activity and stability have potential application prospects in large-scale electrochemical water splitting.

Experimental section

Materials

$Ni(NO_3)_2{\cdot}H_2O$, $Cr(NO_3)_3{\cdot}9H_2O$ and urea were purchased from Macklin. All reagents were of analytical grade and were used without further purification. Deionized water was used throughout the experiments. Ni foam (NF) was used as a substrate. The NF needs to be pretreated to remove the surface oxidation layer. Firstly, the NF was washed in an ultrasonic bath of acetone for 10 min. Subsequently, it was soaked in HCl solution (3 M) for 3 min, and then rinsed with deionized water and ethanol 3 times, respectively.

Synthesis of NiCr-LDH/NF

NiCr-LDHs on NF were synthesized by a one-step hydrothermal reaction. Typically, $Ni(NO_3)_2{\cdot}H_2O$ (0.6 mmol) and $Cr(NO_3)_3{\cdot}9H_2O$ with different ratios (1 : 1, 2 : 1, 3 : 1 and 4 : 1) and urea (2 mmol) were dissolved in 15 mL of deionized water to form a homogeneous solution, then transferred into a 23 mL Teflon-lined stainless-steel autoclave containing a piece of cleaned NF (1 cm × 2 cm) and then hydrothermally treated at 120 °C for 12 h. Finally, the autoclave was cooled down to room temperature. The resulting brownish green sample on NF was washed with ethanol and dried naturally in air overnight. The mass loading of final NiCr-LDH products on the NF was about 2 mg cm^{-2}.

Synthesis of $Ni(OH)_2$/NF and $Cr(OH)_3$/NF

$Ni(OH)_2$ on Ni foam were produced by a hydrothermal method according to a previous report.[26] The synthesis of $Cr(OH)_3$ was similar to that of $Ni(OH)_2$.

Fabrication of RuO_2 and Pt/C on Ni foam

5 mg of RuO_2 or Pt/C powder was dispersed in 50 μL of 5 wt% Nafion and 250 μL of ethanol followed by sonication for 30 min. Then, 10 μL of the catalyst ink was loaded on Ni foam (1 cm × 2 cm) and dried at 70 °C for 1 hour.

Characterization

Powder X-ray diffraction (XRD) patterns of all the samples were obtained using graphite-filtered Cu Kα radiation operating at 40 kV and 30 mA, λ = 0.15418 nm (Shimadzu XRD-6000 diffractometer). Scanning electron microscopy (SEM) with an accelerating voltage of 20 kV (SEM, Zeiss SUPRA 55) was applied for detailed morphology analyses. X-ray photoelectron spectrometry (XPS) was performed using Al Kα radiation (Thermo VG ESCALAB MK II). The positions of all BEs were calibrated by using the C 1s line at 284.8 eV. Transmission electron microscopy (TEM) and energy dispersive X-ray spectroscopy (EDS) mappings were obtained using microscopy (JEOL JEM-2010F) combined with EDX (Oxford X-MaxN 80-TLE) spectroscopy. For TEM observation, the samples were scraped from the Ni foam substrate and ultrasonically dispersed in ethanol and then a drop of the suspension was deposited onto a carbon-coated Cu grid followed by the evaporation of solvent in air.

Electrochemical measurements

Electrochemical measurements were conducted on a CHI 660E electrochemical workstation (CH Instruments Co. USA) with an electrolyte solution of 1.0 M KOH (the electrolyte was degassed by bubbling nitrogen for 30 min), using a standard three-electrode system with NiCr-LDH/NF (1 cm × 1 cm) as the working electrode, a Pt wire (2 cm) as the counter electrode and an Ag/AgCl electrode as the reference electrode.

Commercial Pt/C and RuO_2 were used as references for comparing the electrocatalytic performance of various samples. All potentials measured in this work were referenced to the reversible hydrogen electrode (RHE) scale on the basis of the Nernst equation: $E_{RHE} = E_{Ag/AgCl} + 0.197 + 0.059$ pH. Linear sweep voltammetry (LSV) was performed at 5 mV s^{-1} to obtain the polarization curves and Tafel plots. The stability test was performed using chronopotentiometric measurements. The electrochemical surface area (ECSA) was measured using cyclic voltammetry (CV) in a non-faradaic potential range at various scan rates including 10, 20, 30, 40, 60, and 80 mV s^{-1}. The overall water splitting was performed using a two-electrode configuration using NiCr-LDH/NF as both the anode and cathode.

The turnover frequency (TOF) values are calculated from the equation:

$$\mathrm{TOF} = \frac{I}{4 \times F \times m}$$

where I is the measured current at a certain overpotential, F is the Faraday constant with a value of 96 485 C mol^{-1}, and m is the number of moles of the metal on the electrodes.

Electrochemical impedance spectroscopy (EIS) measurements were performed at a potential of 1.73 V (*vs.* RHE) with frequency ranging from 100 kHz to 0.1 Hz in a N_2-saturated 1 M KOH solution.

Structural model and DFT calculation

The space group of the LDHs is *R*3*m*, with unit cell parameters: $\alpha = \beta = 90°$, $\gamma = 120°$. The supercell of the octahedral layer has 12 metal atoms and 24 OH groups and the distance between the adjacent metal atoms is 3.05 Å. The ratio of Ni/Cr is 2 : 1, which is similar to the experimental result. The supercell is 4 × 3 × 1 in the *a*-, *b*- and *c*-direction, and two CO_3^{2-} are localized on LDH in each model. All calculations were performed with the periodic density functional theory (DFT) method using the CASTEP module in the Material Studio software package.[58] The configurations were optimized at the generalized gradient approximation (GGA) Perdew–Burke–Ernzerhof (PBE) level.[59]

Conflicts of interest

There are no conflicts to declare.

Acknowledgements

This work was supported by the 973 Program (2014CB932103), the National Natural Science Foundation of China (21473013 and 21771021), the Beijing Nova Program (xx2018115), the Fundamental Research Funds for the Central Universities, and the Analytical and Measurements Fund of Beijing Normal University.

Notes and references

1 J. A. Turner, *Science*, 2004, **305**, 972–974.
2 Z. W. Seh, J. Kibsgaard, C. F. Dickens, I. Chorkendorff, J. K. Nørskov and T. F. Jaramillo, *Science*, 2017, **355**, 4998–5009.
3 J. Greeley, T. F. Jaramillo, J. Bonde, I. Chorkendorff and J. K. Nørskov, *Nat. Mater.*, 2006, **5**, 909–913.
4 N. T. Suen, S. F. Hung, Q. Quan, N. Zhang, Y. J. Xu and H. M. Chen, *Chem. Soc. Rev.*, 2017, **46**, 337–365.
5 Z. F. Huang, J. Wang, Y. Peng, C. Y. Jung, A. Fisher and X. Wang, *Adv. Energy Mater.*, 2017, **7**, 1700544.
6 R. Chen, C. Yang, W. Cai, H. Wang, J. Miao, L. Zhang, S. Chen and B. Liu, *ACS Energy Lett.*, 2017, **2**, 1070–1075.
7 Y. Zhao, X. Zhang, X. Jia, G. I. N. Waterhouse, R. Shi, X. Zhang, F. Zhan, Y. Tao, L. Z. Wu, C. H. Tung, D. O. Hare and T. Zhang, *Adv. Energy Mater.*, 2018, 1703585.
8 S. Zhao, R. Jin, H. Abroshan, C. Zeng, H. Zhang, S. D. House, E. Gottlieb, H. J. Kim, J. C. Yang and R. Jin, *J. Am. Chem. Soc.*, 2017, **139**, 1077–1080.
9 L. Yao, N. Zhang, Y. Wang, Y. Nia, D. Yan and C. Hu, *J. Power Sources*, 2018, **374**, 142–148.
10 Y. Wang, Y. Zhang, Z. Liu, C. Xie, S. Feng, D. Liu, M. Shao and S. Wang, *Angew. Chem., Int. Ed.*, 2017, **56**, 5867–5871.
11 Y. Li, L. Zhang, X. Xiang, D. Yan and F. Lia, *J. Mater. Chem. A*, 2014, **2**, 13250–13258.
12 R. Gao and D. Yan, *Nano Res.*, 2018, **11**, 1883–1894.
13 M. Shao, R. Zhang, Z. Li, M. Wei, D. G. Evans and X. Duan, *Chem. Commun.*, 2015, **51**, 15880–15893.
14 Y. Ni, L. Yao, Y. Wang, B. Liu, M. Cao and C. Hu, *Nanoscale*, 2017, **9**, 11596–11604.
15 W. Zhu, L. Liu, Z. Yue, W. Zhang, X. Yue, J. Wang, S. Yu, L. Wang and J. Wang, *ACS Appl. Mater. Interfaces*, 2017, **9**, 19807–19814.
16 X. Yu, M. Zhang, W. Yuan and G. Shi, *J. Mater. Chem. A*, 2015, **3**, 6921–6928.
17 C. Zhang, M. Shao, L. Zhou, Z. Li, K. Xiao and M. Wei, *ACS Appl. Mater. Interfaces*, 2016, **8**, 33697–33703.
18 Z. Lu, W. Xu, W. Zhu, Q. Yang, X. Lei, J. Liu, Y. Li, X. Sun and X. Duan, *Chem. Commun.*, 2014, **50**, 6479–6482.
19 H. Yang, S. Luo, Y. Bao, Y. Luo, J. Jin and J. Ma, *Inorg. Chem. Front.*, 2017, **4**, 1173–1181.
20 W. Liu, J. Bao, M. Guan, Y. Zhao, J. Lian, J. Qiu, L. Xu, Y. Huang, J. Qian and H. Li, *Dalton Trans.*, 2017, **46**, 8372–8376.
21 W. Ma, R. Ma, J. Wu, P. Sun, X. Liu, K. Zhou and T. Sasaki, *Nanoscale*, 2016, **8**, 10425–10432.
22 Z. Lu, L. Qian, Y. Tian, Y. Li, X. Sun and X. Duan, *Chem. Commun.*, 2016, **52**, 908–911.
23 Y. Zhao, X. Jia, G. Chen, L. Shang, G. I. N. Waterhouse, L. Z. Wu, C. H. Tung, D. O'Hare and T. Zhang, *J. Am. Chem. Soc.*, 2016, **138**, 6517–6524.
24 K. Fan, H. Chen, Y. Ji, H. Huang, P. M. Claesson, Q. Daniel, B. Philippe, H. Rensmo, F. Li, Y. Luo and L. Sun, *Nat. Commun.*, 2016, **7**, 11981–11989.

25 T. Tang, W. Jiang, S. Niu, N. Liu, H. Luo, Y. Chen, S. Jin, F. Gao, L. Wan and J. Hu, *J. Am. Chem. Soc.*, 2017, **139**, 8320–8328.
26 J. Luo, J. H. Im, M. Mayer, M. Schreier, M. Nazeeruddin, N. G. Park, S. Tilley, H. Fan and M. Grätzel, *Science*, 2014, **345**, 1593–1596.
27 A. Sivanantham, P. Ganesan and S. Shanmugam, *Adv. Funct. Mater.*, 2016, **26**, 4661–4672.
28 C. Xiao, Y. Li, X. Lu and C. Zhao, *Adv. Funct. Mater.*, 2016, **26**, 3515–3523.
29 Y. Tang, X. Fang, X. Zhang, G. Fernandes, Y. Yan, D. Yan, X. Xiang and J. He, *ACS Appl. Mater. Interfaces*, 2017, **9**, 36762–36771.
30 J. Hou, Y. Wu, S. Cao, Y. Sun and L. Sun, *Small*, 2017, **13**, 1702018.
31 M. S. Burke, L. J. Enman, A. S. Batchellor, S. Zou and S. W. Boettcher, *Chem. Mater.*, 2015, **27**, 7549–7558.
32 L. Wang, C. Lin, F. Zhang and J. Jin, *ACS Nano*, 2014, **8**, 3724–3734.
33 J. Chen, X. Wang and Z. Gong, *J. South China Univ. Technol.*, 2005, **12**, 59–64.
34 C. Dong, X. Yuan, X. Wang, X. Liu, W. Dong, R. Wang, Y. Duanc and F. Huang, *J. Mater. Chem. A*, 2016, **4**, 11292–11298.
35 Y. Yang, L. Dang, M. J. Shearer, H. Sheng, W. Li, J. Chen, P. Xiao, Y. Zhang, R. J. Hamers and S. Jin, *Adv. Energy Mater.*, 2018, **8**, 1703189.
36 G. Chen, T. Wang, J. Zhang, P. Liu, H. Sun, X. Zhuang, M. Chen and X. Feng, *Adv. Mater.*, 2018, **30**, 1706279.
37 G. Jia, Y. Hu, Q. Qian, Y. Yao, S. Zhang, Z. Li and Z. Zou, *ACS Appl. Mater. Interfaces*, 2016, **8**, 14527–14534.
38 X. Xu, H. Liang, F. Ming, Z. Qi, Y. Xie and Z. Wang, *ACS Catal.*, 2017, **7**, 6394–6399.
39 C. Qiu, J. Jiang and L. Ai, *ACS Appl. Mater. Interfaces*, 2016, **8**, 945–951.
40 C. S. Lim, C. K. Chua, Z. Sofer, K. Klímoá, C. Boothroyd and M. Pumera, *J. Mater. Chem. A*, 2015, **3**, 11920–11929.
41 J. Yang, A. G. Baker, H. Liu, W. N. Martens and R. L. Frost, *J. Mater. Chem.*, 2010, **45**, 6574–6585.
42 Y. Xu, W. Tu, B. Zhang, S. Yin, Y. Huang, M. Kraft and R. Xu, *Adv. Mater.*, 2017, **29**, 1605957.
43 L. Yan, L. Cao, P. Dai, X. Gu, D. Liu, L. Li, Y. Wang and X. Zhao, *Adv. Funct. Mater.*, 2017, **27**, 1703455.
44 M. Ledendecker, S. K. Calderón, C. Papp, H.-P. Steinrück, M. Antonietti and M. Shalom, *Angew. Chem., Int. Ed.*, 2015, **127**, 12538–12542.
45 H. Shi, H. Liang, F. Ming and Z. Wang, *Angew. Chem., Int. Ed.*, 2017, **129**, 588–592.
46 H. Wang, H. W. Lee, Y. Deng, Z. Lu, P. C. Hsu, Y. Liu, D. Lin and Y. Cui, *Nat. Commun.*, 2015, **6**, 7261–7268.
47 L. L. Feng, G. Yu, Y. Wu, G. D. Li, H. Li, Y. Sun, T. Asefa, W. Chen and X. Zou, *J. Am. Chem. Soc.*, 2015, **137**, 14023–14026.
48 X. Li, G. Han, Y. Liu, B. Dong, W. Hu, X. Shang, Y. Chai and C. Liu, *ACS Appl. Mater. Interfaces*, 2016, **8**, 20057–20066.
49 B. Dong, K. Yan, Z. Liu, J. Chi, W. Gao, J. Lin, F. Dai, Y. Chai and C. Liu, *J. Electrochem. Soc.*, 2018, **165**, 102–108.
50 O. Diaz-Morales, D. Ferrus-Suspedra and M. T. M. Koper, *Chem. Sci.*, 2016, **7**, 2639–2645.
51 X. Gao, H. Zhang, Q. Li, X. Yu, Z. Hong, X. Zhang, C. Liang and Z. Lin, *Angew. Chem., Int. Ed.*, 2016, **55**, 6290–6294.
52 X. Cui, P. Ren, D. Deng, J. Deng and X. Bao, *Energy Environ. Sci.*, 2016, **9**, 123–129.
53 O. Diaz-Morales, I. Ledezma-Yanez, M. T. M. Koper and F. Calle-Vallejo, *ACS Catal.*, 2015, **5**, 5380–5387.
54 A. S. Batchellor and S. W. Boettcher, *ACS Catal.*, 2015, **5**, 6680–6689.
55 M. S. Islam, M. Kim, X. Jin, S. M. Oh, N. Lee, H. Kim and S. Hwang, *ACS Energy Lett.*, 2018, **3**, 952–960.
56 C. Tang, N. Cheng, Z. Pu, W. Xing and X. Sun, *Angew. Chem., Int. Ed.*, 2015, **127**, 9483–9487.
57 Y. P. Zhu, Y. P. Liu, T. Z. Ren and Z. Y. Yuan, *Adv. Funct. Mater.*, 2015, **25**, 7337–7347.
58 M. Segall, P. Linda, M. Probert, C. Pickard, P. Hasnip, S. Clark and M. Payne, *Materials studio CASTEP, version 2.2*. Accelrys, San Diego, CA, 2002.
59 S. Xu, T. Pan, Y. Dou, H. Yan, S. Zhang, F. Ning, W. Shi and M. Wei, *J. Phys. Chem. C*, 2015, **119**, 18823–18834.